Optics Letters

Mid-infrared quantum cascade laser-based structured illumination microscope

M. Le,[1] O. Myers,[1] J. Squier,[2,3,4] and Y. Phal[1,3,4,5,*]

[1]Department of Electrical Engineering, Colorado School of Mines, 1500 Illinois St., Golden, Colorado 80401, USA
[2]Department of Engineering Physics, Colorado School of Mines, 1500 Illinois St., Golden, Colorado 80401, USA
[3]Quantitative Biosciences and Engineering Program, Colorado School of Mines, Golden, Colorado 80401, USA
[4]Quantum Engineering Program, Colorado School of Mines, Golden, Colorado 80401, USA
[5]Colorado Clinical Translational Sciences Institute (CCTSI), Aurora, Colorado 80045, USA
*yphal@mines.edu

Received 4 November 2025; revised 25 March 2026; accepted 16 April 2026; posted 21 April 2026; published 5 May 2026

We demonstrate, for the first time to the best of our knowledge, the implementation of Spatial Frequency Modulated Imaging (SPIFI) microscopy in the mid-infrared region using a Quantum Cascade Laser (QCL) source. Hyperspectral imaging in the mid-infrared (3–20 μm) enables chemically specific mapping and structural imaging based on molecular contrast, which is otherwise inaccessible in the visible or near-infrared region. But mid-infrared microscopes are often limited by slow raster scanning and costly detector arrays. Our approach uses spatial frequency-encoded structured illumination and a low-cost single-pixel mid-infrared detector to acquire hyperspectral images in transflection mode. The system—structured illumination single-pixel imaging system in the mid-infrared—provides a practical trade-off between speed and complexity, offering acquisition speeds comparable to selected QCL-based point-scanning implementations, while maintaining a simple, cost-effective optical design utilizing off-the-shelf components. We present a preliminary resolution measurement as well as absorption images of coronal sections of a mouse brain at both 6 and 7 μm, demonstrating chemically selective contrast and robust image formation suitable for future high-resolution and compressive implementations.

https://doi.org/10.1364/OL.583804

Introduction. Quantum Cascade lasers, since their invention in the early 1990s [1], have proven to be an invaluable technology for replacing coherent broadband infrared sources. The increasing availability and quality of broad-spectrum QCLs has allowed classically visible and near-infrared spectral imaging techniques to be adapted to the molecular fingerprint region (3–20 μm) [2,3]. QCLs have been implemented to reduce scan times and generate high-quality absorption spectra for chemical imaging [4,5] and chiral analysis [6–8], improve contrast in hyperspectral infrared absorption microscopy [2], and even enable chiral imaging [3].

Recent advancements have sought to overcome these limitations through several innovative approaches. One promising method, Upconversion Imaging, utilizes optically nonlinear media such as PPLN, UCNPs, or TTA to shift mid-IR light into the visible (VIS) or near-infrared (NIR) spectrum [9]. By combining low-energy mid-IR photons with a high-energy pump source within these media, the signal can be captured using standard, cost-effective CCD or CMOS detectors. Parallel to this, Optical Photothermal Infrared (O-PTIR) imaging has emerged as a widely adopted commercial technique. O-PTIR employs a mid-IR QCL as a pump and a visible laser as a probe to detect localized changes in a material's refractive index through the photothermal effect [10]. By measuring these fluctuations, the system maps the sample's absorption with a spatial resolution dictated by the diffraction limit of the visible probe laser. This allows the technique to effectively bypass the traditional diffraction limits associated with mid-IR illumination by leveraging a visible probe beam. Additionally, approaches based on non-degenerate two-photon absorption (NTA) have gained attention for enabling mid-IR detection with readily available silicon-based detectors. In this scheme, a mid-IR photon is absorbed simultaneously with a higher-energy near-IR photon, allowing their combined energy to exceed the detector bandgap. This permits indirect detection of mid-IR signals using mature silicon-based sensor technology, offering a complementary route to cost-effective and high-resolution imaging [11–13]. Improvements to raster-scanning topologies have also been explored in depth to improve single-pixel detector scanning speeds. Methods utilizing dual comb mid-infrared sources encode spectroscopic information into the RF domain, reducing pixel dwell times and providing per pixel spectroscopic information [14,15]. These techniques also allow for the use of non-QCL-based near-infrared illumination sources such as lithium-niobate lasers [15].

Despite these advances, mid-infrared microscopy continues to face a fundamental challenge: the scarcity of affordable, high-pixel-count detector arrays that are natively sensitive across the biologically relevant 3–8 μm band.

As a result, most mid-IR imaging systems rely on raster scanning or interferometric detection, which provide high spectral

fidelity but at the cost of long acquisition times and mechanical complexity [2,3,10]. Array-based systems, while faster, are often prohibitively expensive and suffer from limited well depth and noise [16]. There remains a need for imaging architectures based on structured illumination schemes that balance chemical specificity, acquisition speed, and instrumental simplicity.

Spatial frequency modulated imaging (SPIFI) addresses these needs by encoding spatial information into temporal modulation frequencies detected by a single-pixel sensor. Originally demonstrated in the visible regime, SPIFI enables multiplexed image formation [17,18] without mechanical rastering. Extending this principle to the mid-infrared presents unique advantages: compatibility with single-element detectors and a simplified optical design.

SPIFI encodes spatial information into a temporal frequency spectrum detected by a single-element photodetector. In this scheme, a rotating or translating mask with a spatially varying transmission pattern introduces a time-dependent spatial frequency onto the illumination beam. As the mask modulates the incident field, spatial features in the sample are heterodyned into distinct temporal frequencies, allowing image reconstruction from a single temporal signal. This method differs from typical single-pixel confocal microscopy in that a singular line image is generated without the need to scan the illumination source or detector.

The fundamental theory and operating principles of SPIFI have been discussed in great detail in previous works [17,19,20]. Briefly, a light sheet (cursor) is spatially modulated via a binarized mask (SPIFI mask) with a variable spatial frequency pattern according to $M(x,t) = \frac{1}{2}\{1 + \cos[2\pi f_x(t)x]\}$, where $f_y(t)$ can be further parametrized by the linear chirp factor, k, and offset frequency f_0 such that $f_y(t) = f_0 + k(t)$. We present the Cartesian form of this equation, as used in similar works [17]; however, other literature references the typical polar equation used for spinning reticle masks [21]. The SPIFI mask is machined as a binary mask with a typical 50% duty cycle, yielding the following transfer function $M(x,t) = (1 + \text{sign}\{\cos[2\pi f_x(t)x]\})/2$. The mask also acts as a variable diffraction grating, with diffracted orders propagating after the mask and onto the sample plane. The mask modulated electric field (in x) at the detection plane after interacting with the sample complex field $C(y)$ can be represented by the following intensity field:

$$I_m(x,t) = I(x)\frac{1}{8}\{3 + 4\cos[2\pi f_x(t)x] + \cos[2\pi 2 f_x(t)x]\}C(y). \quad (1)$$

$I(x)$ corresponds to the intensity of the incident electric field from the illumination source, while the two cos terms correspond to the spatial frequencies present in the reconstructed image. A key advantage is that sequential-mode SPIFI enables extended source imaging with single element detection, as compared to point sources and raster scanning. The optical resolution is determined by the highest spatial frequency encoded by the mask and the system's numerical aperture. In the visible linear excitation regime, SPIFI has demonstrated up to twofold enhancement beyond the conventional coherent diffraction limit [17,18]. In this work, we focus on establishing the mid-IR implementation and demonstrating its capability for chemically specific, label-free imaging, deferring resolution-extended variants to future studies.

In practice, image retrieval and reconstruction using SPIFI is relatively straightforward, as presented in Fig. 1. A complete

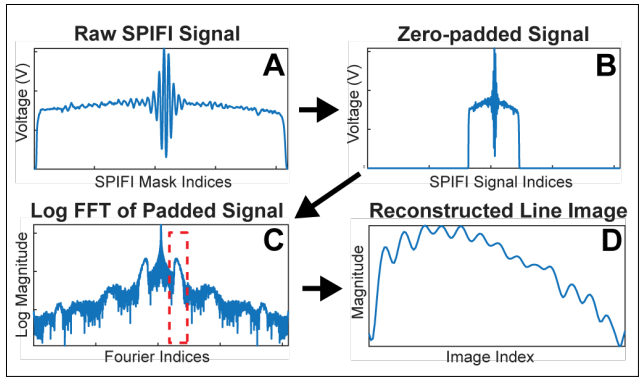

Fig. 1. A typical SPIFI image processing workflow. The initial signal is taken (A). The signal is then zero-padded to be a length of 2^n to allow for a proper FFT (B). A FFT is then performed (C). The respective 1st order SPIFI peak corresponding to a spot-size limited image is then isolated from the FFT (D). This isolated order contains the reconstructed image.

scan across the Cartesian SPIFI mask is captured and isolated, Fig. 1(A). It is important to note that the signal is collected assuming a constant traversal across the mask, either in time or distance interval. The signal is then padded and centered in the original capture domain to the nearest length 2^n, Fig. 1(B). Larger padding lengths may be used to allow for higher spatial frequencies present in the data set to be preserved. A fast Fourier transform (FFT) is then performed on the padded signal, Fig. 1(C). We can see that multiple SPIFI peaks are present, each of order $2nf_0$ where f_0 is the central frequency of the first order image. A single SPIFI order is then isolated, yielding an image corresponding to the ith order line image, Fig. 1(D). Further phase, flattening, and filtering can then be performed to correct the image, as illustrated in [17]; however, for brevity of this paper, we simply apply a flattening field $R(y)$ to compensate for the Gaussian intensity profile inherent to coherent illumination sources.

Optical system and experimental setup. While several novel implementations of SPIFI exist, as elucidated in previous sections, many hurdles exist when translating visible-light systems into the mid-infrared. In order to improve cost-effectiveness, minimize optical elements, and improve testing flexibility, the following schema was developed as presented in Fig. 2. The system consists of 3 distinct optical groups: 1) beam expansion, collimation, and leveling; 2) SPIFI modulation and imaging; and 3) collection.

The QCL illumination source (Daylight Solutions DRS MIRcat) is leveled via gold-plated mirrors (Thorlabs PF10-03-M01) and collimated and expanded 2× via a simple achromat telescope (Thorlabs AC254-050-E, AC254-100-E). The laser was specifically chosen for its desirable output characteristics (low M^2, gapless tunability from 5 to 12 μm). The expanded beam then passes through a cylindrical lens to form the light sheet (Thorlabs LJ7003RM-E3). A one-to-one imaging system then projects the light sheet onto the spatial modulation mask (MASK, custom etched silver-plated mirror) and refocuses it onto the sample plane. The beam then passes through a second cylindrical lens (Thorlabs LJ7003RM-E3) positioned at 90° relative to the first cylindrical lens, and a collimation lens (Thorlabs LA7228-E3) to allow for all of the light to be incident on the detector (Vigo Photonics PVI-4TE MCT).

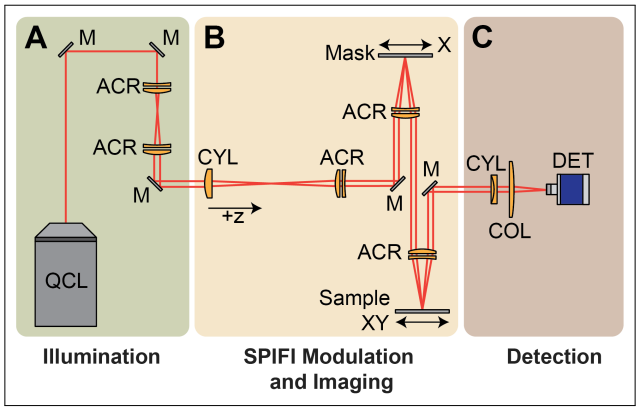

Fig. 2. SPIFI optical component layout. The system schematic is divided into three stages: (A) illumination, (B) spatial modulation and imaging, and (C) detection. The illumination source, a quantum cascade laser (QCL, Daylight Solutions DRS MIRcat), is leveled via gold-plated mirrors (M, Thorlabs PF10-03-M01) and collimated and 2× expanded via a simple achromat telescope (ACR, Thorlabs AC254-050-E, AC254-100-E). The expanded beam then passes through a cylindrical lens to form the light sheet (CYL, Thorlabs LJ7003RM-E3). A one-to-one imaging system then projects the light sheet onto the spatial modulation mask (MASK, custom etched silver-plated mirror), and refocused onto the sample plan (Sample, mid-IR BaF_2 slides, Kevley Technologies). The beam is then passed through a second cylindrical lens (CYL, Thorlabs LJ7003RM-E3) positioned at 90° relative to the first cylindrical lens, and a collimation lens (COL, Thorlabs LA7228-E3) to allow for all of the light to be incident on the detector (DET, Vigo Photonics PVI-4TE MCT).

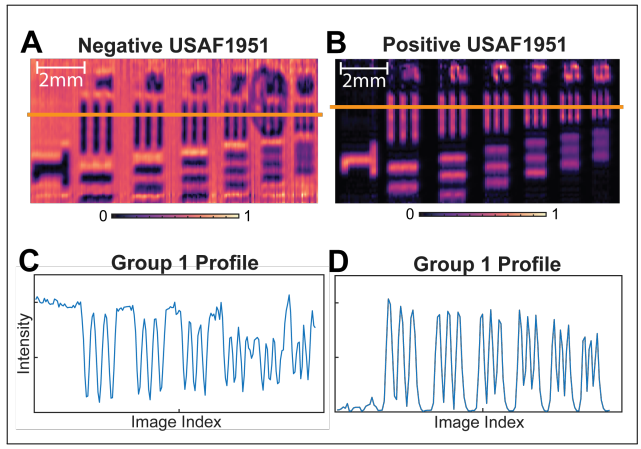

Fig. 3. Resolution measurements using negative (A) and positive (B) USAF 1951 test targets (Thorlabs R3L3S1N, R3L3S1P). The smallest resolvable feature is Group 1, element 6, corresponding to 3.56 lp/mm. While smaller feature sizes are differentiable, we report a best spatial resolution of 3.56 lp/mm in the first-order image reconstruction.

Both the SPIFI mask and sample are controlled via precision linear actuators (Thorlabs MTS25-Z8). Due to the MIRcat QCL operating in a pulsed mode at the desired wavelengths, the detector is coupled to a digital lock-in amplifier (Zurich Instruments MFLI 500 kHz) and demodulated via the square wave trigger output of the QCL. The demodulated signal is then digitized via DAC (Spectrum Instrumentation M4i.4450-x8). All data acquisition is performed via a single PC and automated via custom Python scripting. Image retrieval and post-processing are all performed in MATLAB.

The optical system was designed in Ansys Zemax OpticsStudio. Simulation reports a limiting spot size at the sample plane of 126 µm with a limiting aperture of 4 mm imposed by the expanded beam size and clearance constraints of the optical system.

Results. Spatial resolution was characterized using standardized USAF 1951 resolution targets (Thorlabs R3L3S1N and R3L3S1P). Representative images are shown in Fig. 3. While many images were taken across multiple sectors of the test target, Group 1 of the USAF 1951 target was the smallest group that yielded adequate contrast across the entirety of the group. Group 1, element 6 was readily resolved in both positive and negative targets, yielding a resolution of 3.56 lp/mm ≈ 140 µm. The calculated minimum cursor width (analogous to spot size at the mask and sample planes) via Zemax ray tracing software yielded 126 µm, calculated with a Gaussian beam propagation model matched to our illumination source. However, effective resolution of the system is limited by the SPIFI mask, which, in this configuration, does not fill the entire pupil of the excitation optic. Further degradation in performance was likely attributed to a missed focus on either the mask or the sample planes. Improved focusing and calibration procedures are expected to bring the performance closer to the theoretical limit.

Acquisition time for a single line image is limited by the maximum linear stage velocity of 2.5 mm/s. For a 15 mm wide machined mask, this corresponds to an image scan time of 6 s per line scan. With a linear FOV of ≈ 4 mm, the maximum acquisition time for a 4 mm × 4 mm image is 174 s (10.88 s/mm^2) using a horizontal step spacing equal to the line cursor width, placing the current architecture on par with the fastest commercial raster scanning mid-IR microscopes (10 s/mm^2), and offering about 15× improvement over a conventional stage-scanning architecture (150 s/mm^2). At current scan speeds, as referenced in Fig. 3, we report a spatial resolution of 3.56 lp/mm. The use of mid-IR achromatic lenses has also allowed gapless wavelength tuning between the 6 and 7 µm region without refocusing, demonstrating the system's inherent achromatic stability. However, as the design spot size and performance approach the diffraction limit, considerations must be made for chromatic focal shift and will be incorporated into future designs.

Hyperspectral reflection-mode images of mouse brain tissue were acquired using the custom-built SPIFI imaging system to evaluate the system performance under realistic biological imaging conditions (Fig. 4). Samples consisted of CD-1 mouse brain coronal paraffin sections (Zyagen, San Diego, CA) mounted on low-emission (low-E) reflective slides (Kevley Technologies, Chesterland, OH). For preliminary demonstration of the developed platform, imaging was performed sequentially at 6 and 7 µm wavelengths, selected based on characteristic vibrational bands of proteins and lipids. The sample focus was fixed at 7 µm and held constant when switching to 6 µm, thereby validating the system's ability to capture chemically distinct contrast without refocusing.

The images presented show the absorption contrast (A) of the material, computed as, $A = -\log_{10}(I/I_0)$ where I_0 is the incident light intensity and I is the reflected intensity of the sample. It is evident that a strong absorption band at ≈ 6 µm is present in the mouse brain, consistent with protein amide and CH stretching

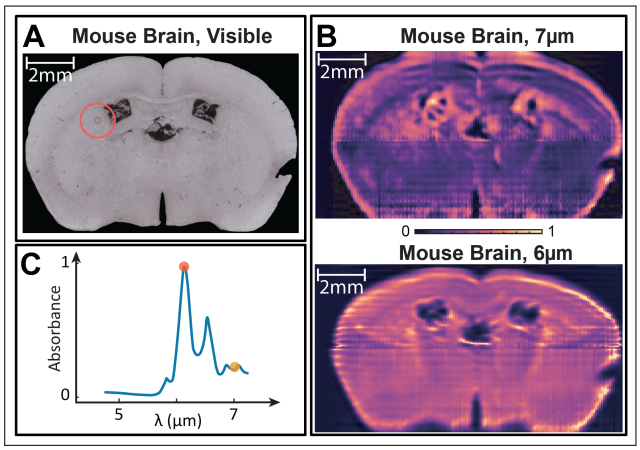

Fig. 4. Reflection-mode composite images of a mouse brain section acquired using both a (A) conventional optical microscope, as well as our (B) custom-built mid-IR QCL-SPIFI system. Hyperspectral absorption imaging capability as shown at two different wavelengths, 6 and 7 μm. Individual mid-IR images were mosaicked from two 4 mm × 15 mm scans following FFT-based reconstruction and field flattening processes. (C) Absorption spectra of the brain tissue via QCL absorption spectroscopy, with 6 and 7 μm absorbance points marked.

bands in biological tissue, Fig. 4(C), and corroborated further by the full absorption spectra of the sample for chemical identification. Further contrast enhancement can be applied to the image for more in-depth structure characterization. It is evident from both images in Fig. 4(B) that a fundamental horizontal banding is present. This artifact is most likely attributed to rasterization or coarseness features on the machined SPIFI mask, or noise introduced by the scanning architecture. These artifacts can be mitigated through refined mask fabrication and post-processing corrections.

Conclusion. In this work, we demonstrate the first mid-IR realization of SPIFI microscopy using a QCL source, establishing a foundation for fast, chemically specific imaging and future resolution-enhanced architectures. The single-pixel design achieves a spot-size limited resolution of ~140 μm, which is within initial design limits and predicted performance metrics of the system, while delivering acquisition speeds comparable to state-of-the-art commercial scanning systems. Furthermore, we performed reflection-mode imaging of mouse brain tissue sections at 6 and 7 μm, showing differential absorption of biological material, confirming the system's capability for chemical-specific imaging without refocusing, and validating its use for hyperspectral imaging in the mid-IR.

These results establish the foundation for a new class of single-pixel structured illumination architectures in the mid-IR that balance spectral fidelity, acquisition speed, and affordability; suitable for biomedical and chemical microscopy applications. Future work will focus on improving optical design, alignment, and calibration procedures to reach the diffraction limit, extending the technique to broadband hyperspectral operation, and incorporating faster scanning architectures for real-time imaging.

Funding. Division of Translational Impacts (2414684); Science Mission Directorate (23-PICASSO23-0026).

Acknowledgment. This material is based upon work supported by the National Science Foundation Partnership for Innovation Program via Grant No. 2414684. Y.P. acknowledges financial support from the National Science Foundation Partnership for Innovation Program via Grant No. 2414684 and the National Aeronautics and Space Administration PICASSO program via Grant No. 23-PICASSO23-0026.

Disclosures. The authors declare no conflicts of interest.

Data availability. Data underlying the results presented in this paper are not publicly available at this time but may be obtained from the authors upon reasonable request.

REFERENCES

1. J. Faist, F. Capasso, D. L. Sivco, *et al.*, Science **264**, 553 (1994).
2. Y. Phal, K. Yeh, and R. Bhargava, Appl. Spectrosc. **75**, 1067 (2021).
3. Y. Phal, K. Yeh, and R. Bhargava, Anal. Chem. **93**, 1294 (2021).
4. J. Helbing and M. Bonmarin, J. Chem. Phys. **131**, 174507 (2009).
5. S. Lüdeke, M. Pfeifer, and P. Fischer, J. Am. Chem. Soc. **133**, 5704 (2011).
6. A. Utyushev, I. L. Rasskazov, and Y. Phal, Anal. Chem. **98**, 10584 (2026).
7. V. A. Norvick, M. Le, E. Modesitt, *et al.*, ACS Meas. Sci. Au **5**, 729 (2025).
8. M. Le, V. A. Norvick, L. Nafie, *et al.*, Annu. Rev. Anal. Chem. **19** 15.1 (2026).
9. J. S. Dam, P. Tidemand-Lichtenberg, and C. Pedersen, Nat. Photon. **6**, 788 (2012).
10. D. Zhang, C. Li, C. Zhang, *et al.*, Sci. Adv. **2**, e1600521 (2016).
11. D. Knez, A. M. Hanninen, R. C. Prince, *et al.*, Light Sci. Appl. **9**, 125 (2020).
12. E. O. Potma, D. Knez, M. Ettenberg, *et al.*, APL Photon. **6**, 096108 (2021).
13. D. Knez, B. W. Toulson, A. Chen, *et al.*, Sci. Adv. **8**, eade4247 (2022).
14. G. A. Turner, D. I. Herman, A. Razumtcev, *et al.*, Opt. Exp. **33**, 28290 (2025).
15. P. Chang, R. Ishrak, N. Hoghooghi, *et al.*, APL Photon. **9**, 106111 (2024).
16. A. Rogalski, Prog. Quant. Electron. **36**, 342 (2012).
17. D. Scarbrough, S. Cottrell, J. Czerski, *et al.*, Appl. Opt. **62**, 3861 (2023).
18. S. Cottrell, J. Czerski, D. Adams, *et al.*, Opt. Exp. **31**, 24283 (2023).
19. J. J. Field, K. A. Wernsing, S. R. Domingue, *et al.*, Proc. Natl. Acad. Sci. USA **113**, 6605 (2016).
20. P. Stockton, G. Murray, J. J. Field, *et al.*, Opt. Commun. **520**, 128401 (2022).
21. R. G. Driggers, M. Spie, C. E. Halford, *et al.*, Opt. Eng. **29**, 1398 (1990).